Enzyme-like water preorganization in a synthetic molecular cleft for homogeneous water oxidation catalysis

Niklas Noll,[1] Ana-Maria Krause,[2] Florian Beuerle[1,2] and Frank Würthner[1,2*]

[1] Institut für Organische Chemie, Universität Würzburg, Am Hubland, 97074 Würzburg, Germany

[2] Center for Nanosystems Chemistry (CNC), Universität Würzburg, Theodor-Boveri-Weg, 97074 Würzburg, Germany

*Email: wuerthner@uni-wuerzburg.de

This article has been published in Nature Catalysis:

Noll, N., Krause, A.-N., Beuerle, F. & Würthner, F. Enzyme-like water preorganization in a synthetic molecular cleft for homogeneous water oxidation catalysis. *Nat. Catal.* **5**, 867–877 (2022).

Abstract

Inspired by the proficiency of natural enzymes, mimicking of nanoenvironments for precise substrate preorganisation is a promising strategy in catalyst design. However, artificial examples of enzyme-like activation of H_2O molecules for the challenging oxidative water splitting reaction are hardly explored. Here, we introduce a mononuclear Ru(bda) complex (**M1**, bda: 2,2'-bipyridine-6,6'-dicarboxylate) equipped with a bipyridine-functionalized ligand to preorganize H_2O molecules in front of the metal center as in enzymatic clefts. The confined pocket of **M1** accelerates chemically driven water oxidation at pH 1 by facilitating a water nucleophilic attack pathway with a remarkable turnover frequency of 140 s^{-1} that is comparable to the oxygen-evolving complex of photosystem II. Single crystal X-ray analysis of **M1** under catalytic conditions allowed the observation of a 7th H_2O ligand directly coordinated to a Ru^{III} center. Via a well-defined hydrogen-bonding network, another H_2O substrate is preorganized for the crucial O–O bond formation via nucleophilic attack.

Main

Enzymes as highly efficient natural catalysts have long inspired the field of supramolecular chemistry.[1,2] Initiated by Emil Fischer‘s famous lock-and-key hypothesis in 1894,[3] the importance of a sophisticated design for catalytic pockets in artificial enzyme mimics was manifested early on.[4–6] At the active sites of hydrogenases,[7,8] the cytochrome c oxidases[9,10] or the oxygen-evolving complex of photosystem II (OEC-PSII),[11–13] the surrounding protein domains create a well-defined nanoenvironment, which facilitates substrate preorganization by applying weak non-covalent interactions such as hydrogen bonding or electrostatic interactions.[14] X-ray crystal structure analysis revealed extensive hydrogen-bonding water networks surrounding the active sites of these metalloproteins, which serve as channels for water diffusion and proton transfer to the surrounding bulk solvent.[7–12] In OEC-PSII, the kinetically demanding four-electron oxidation of H_2O into molecular O_2 occurs on the millisecond timescale.[11–13] As key component of PSII, a particular tyrosine-histidine pair acts as proton-coupled redox mediator between the OEC and the nearby light-harvesting chromophore assemblies and alters the hydrogen-bonding environment around the active site.[15]

Inspired by the natural archetype, numerous synthetic mimics of the natural OEC have been reported previously, but typically very low or no catalytic activity and high overpotentials are obtained as such synthetic clusters lack the protein environment.[16,17] Consequently, there is a continuing need for molecular water oxidation catalysts (WOCs) working at low overpotential for sustainable fuel production.[18–20] After the introduction of the ‘blue dimer’ by Meyer *et al.*,[21] ruthenium-based catalysts, especially the Ru(bda) system (bda: 2,2’-bipyridine-6,6’-dicarboxylate),[22,23] have been established as homogenous catalysts with activities comparable to the natural OEC.[24,25] The performance of these artificial WOCs strongly depends on the mechanism for O–O bond formation, where two general pathways are distinguished: water nucleophilic attack (WNA) and interaction of two M-O units (I2M).[26] As a paramount factor to distinguish between these two pathways, second coordination sphere effects by a well-defined ligand framework have been widely applied.[27,28] As an appealing strategy, the activation barrier for the WNA mechanism can be lowered by the presence of an additional base, which acts as a proton-accepting unit and leads to preorganization of incoming H_2O molecules. Intuitively, any intramolecular arrangement should improve catalytic performance compared to the addition of an external base.[29–32] Therefore, the molecular design of confined environments provides the next step towards synthetic enzyme mimics. For example, recent examples showcased a significant rate enhancement in the I2M pathway after inter-catalyst coupling by supramolecular encapsulation of Ru WOCs either within mesoporous silica[33] or a self-assembled Pt nanosphere.[34] Additionally, this concept was also applied to proton reduction catalysts encapsulated in supramolecular cages[35] or metallopolymers[36] which resulted in improved catalytic performance and lower overpotentials. In prior work, we presented multinuclear macrocyclic assemblies, which showed high catalytic performance via WNA pathway by benefiting from cooperative effects between the catalytic centers.[25,27]

In classical transition metal catalysis, the supporting ligands act as spectators and only indirectly modulate catalysis by electronic and steric effects. To closer mimic biological systems, substrate preorganization to the catalytically active metal site by noncovalent interactions (hydrogen bonds, electrostatic interactions, etc.) with a remote recognition unit was applied in different types of transition metal-catalyzed reactions such as hydrogenation,[37,38] hydroformylation,[39,40] C–H activation[41–44] and C–H oxidation reactions.[45,46] For an enzyme-inspired approach, the formation of a confined environment around the active center allows for a more precise positioning of a recognition site for selective substrate preorganization. Until now, such a conceptual design strategy was only reported on selected examples focusing on hydroformylation[47] and proton reduction catalysis[35] but not for water oxidation catalysis.

Here, we introduce a molecular design strategy that incorporates one single catalytic Ru(bda) subunit into a well-defined macrocyclic nanostructure. Accordingly, we present the bioinspired cyclic mononuclear Ru(bda) catalyst **M1**, which is equipped with a proximal base in its ligand framework to facilitate preorganization of substrate water molecules via noncovalent interactions. As a reference, we also synthesized the unsubstituted complex **M2**. Detailed investigations by pH-dependent NMR experiments and H/D kinetic isotope effect (KIE) studies revealed a severe reliance of the mechanistic pathway and catalytic performance of **M1** on the relative spatial orientation of the axial ligand sphere. Under acidic conditions, **M1** reached a turnover frequency (TOF) of 140 s^{-1} per Ru unit via WNA pathway. Single crystal X-ray analysis of **M1** at a predominant Ru^{III} oxidation state gave clear evidence for the formation of a confined space around the catalytic center, which allowed the observation of a 7th H_2O ligand directly coordinated to a Ru^{III} center after acidic catalytic water oxidation. The preorganization of additional hydrogen-bonded H_2O molecules in proximity prepares the system for the crucial water nucleophilic attack and could be additionally confirmed by FT-IR spectroscopy experiments.

Results

Synthesis. Mononuclear Ru(bda) complexes **M1** and **M2**, as synthetic enzyme mimetics (Fig. 1a,b), were synthesized in a two-step procedure (Fig. 1c). The ditopic ligands **L1** and **L2** were obtained via twofold Suzuki-Miyaura reaction between the axial pyridine ligand **1** and central bipyridine (**BP1**) or biphenyl (**BP2**) units, respectively (Synthesis of bidentate ligands in the Methods and Supplementary Note 2). Subsequentially, twofold ligand exchange at $[Ru(bda)(dmso)_2]$ with the respective bidentate ligand gave **M1** or **M2** in 35-49% yield besides higher macrocycles as side products (Synthesis of mononuclear Ru complexes in the Methods and Supplementary Note 3). The mononuclear assemblies were fully characterized by NMR spectroscopy, mass spectrometry, elemental analysis, and X-ray crystallography. The UV-Vis absorption and redox properties comply with previously reported Ru complexes (Supplementary Table 1 & Supplementary Figs. 1–3).[25]

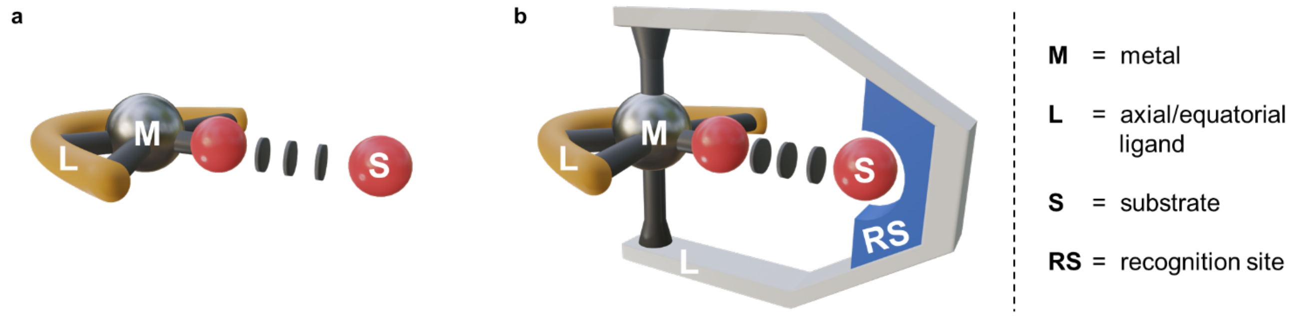

Conventional organometallic catalysis

Enzyme-like control of a confined environment

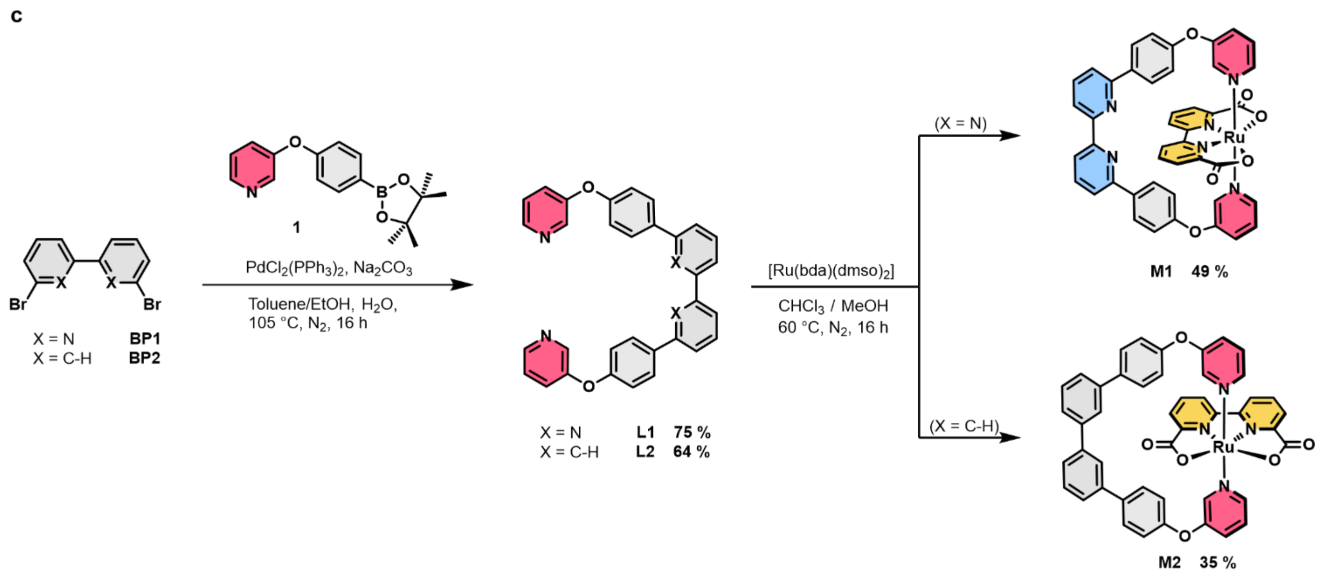

Fig. 1 | Enzyme-mimetic approach and synthesis of mononuclear Ru(bda) complexes. **a**, Conventional organometallic catalysis; **b**, Enzyme-like control of a confined environment with noncovalent interactions between metal center and the substrate indicated by black circles. **c,** Synthesis of mononuclear Ru(bda) complexes **M1** and **M2**. Boronic ester **1** was prepared in two steps starting from commercially available 4-(pyridine-3-yloxy) aniline (Synthesis towards molecular precursor **1** in Methods and Supplementary Note 1).

Catalytic water oxidation. Initially, we tested these Ru(bda) complexes in chemical water oxidation catalysis using cerium ammonium nitrate (CAN) as sacrificial oxidant[48] in acidic aqueous solution

(CH_3CN/H_2O 4:6, pH 1, triflic acid) (Fig. 2a, Supplementary Figs. 6 and 7). The evolved O_2 was monitored by attached pressure sensors in combination with end-point analysis of the gas composition by gas chromatography (GC) of the headspace, which verified O_2 as the only gaseous product generated during catalysis (Supplementary Figs. 8 and 9). For the bipyridine-containing **M1**, the observed linear relationship between the amount of evolved O_2 and the concentration of the catalyst is indicative for the unimolecular WNA mechanism as previously reported for multinuclear macrocycles from our group.[25] Via linear regression, an exceptionally high average TOF value of 140±5 s^{-1} is obtained. In stark contrast, for the unfunctionalized reference **M2**, the initial rates of O_2 evolution were of second order with respect to the catalyst concentration, which is in line with the bimolecular I2M mechanism.[23] Apparently, this switch in the reaction mechanism is accompanied by a significantly lower catalytic performance for **M2** as shown by lower TOF values in the range of 18–54 s^{-1} in the measured concentration range. In addition, these activities also correlate with the obtained TON values as **M1** (TON = 950±50) exhibits an almost two times higher turnover compared to the unfunctionalized reference **M2** (TON = 500±50). Post-catalytic analysis of the reaction mixtures by MALDI TOF mass spectrometry indicated axial ligand dissociation as main degradation pathway (Supplementary Figs. 10 and 11). In order to verify if this mechanistic change is pH-dependent, both complexes were also investigated at neutral conditions. Since the sacrificial oxidant CAN is only stable at low pH,[48] we applied photocatalytic water oxidation in 50 mM phosphate buffered CH_3CN/H_2O 4:6 mixtures at pH 7 (Fig. 2b, Supplementary Figs. 12 and 13 and Photocatalytic Water Oxidation in the Methods). Surprisingly, both complexes showed a second order dependency of the initial O_2 evolution rate on the WOC concentration. Apparently, the reaction kinetics for base-containing **M1** change when going from acidic to neutral conditions. Moreover, the performance is strongly reduced in comparison to reference **M2** as significantly higher concentrations are needed for substantial O_2 generation (c(**M1**) = 5–45 μM and c(**M2**) = 0.5–3 μM, Supplementary Figs. 14 and 15) and a more than one order of magnitude lower catalytic activity is observed with TOFs of 0.4–3.2 s^{-1} and 0.05–0.1 s^{-1} for **M2** and **M1**, respectively. The generally lower TOFs for photocatalytic compared to chemical conditions are most likely attributed to the limited stability of the sacrificial oxidant $[Ru(bpy)_3]^{3+}$ under the applied conditions.[48,49] MALDI TOF mass spectrometry after photocatalysis with either **M1** and **M2** confirmed that the Ru(bda) catalysts were still present, and that photosensitizer degradation is the main deactivation pathway (Supplementary Figs. 16 and 17). Again, the direct correlation between the measured TON (TON(**M1**) = 10±1 and TON(**M2**) = 105±10) and TOF values indicates a much higher stability of reference **M2** under the applied conditions.

For further insight, kinetic isotope effects (KIE) for water oxidation with **M1** and **M2** were studied under both chemical (pH 1) and photocatalytic (pH 7) conditions (for experimental details Kinetic Isotope Experiments in the Methods). For chemical water oxidation, a linear dependency and a KIE of 1.6 was observed for **M1** indicating a WNA mechanism (Supplementary Fig. 18). By contrast, a KIE of 1.0 with a second order dependency indicated the bimolecular I2M mechanism for reference **M2** (Supplementary Fig. 19). Subsequently, KIEs for both **M1** and **M2** were investigated under photocatalytic conditions at pH 7 (Supplementary Figs. 20 and 21). In accordance with the previous results, both **M1** and **M2** displayed the expected quadratic dependency on the catalyst concentration and after linearization, a KIE of around 1.2 was obtained in both cases with similar reaction rates $k(H_2O)$ and $k(D_2O)$. In summary, these results clearly indicate different reactions kinetics and a mechanistic switch for bipyridine-containing catalyst **M1** at either acidic or neutral conditions, which might be induced by different conformations for the bridging macrocycle.

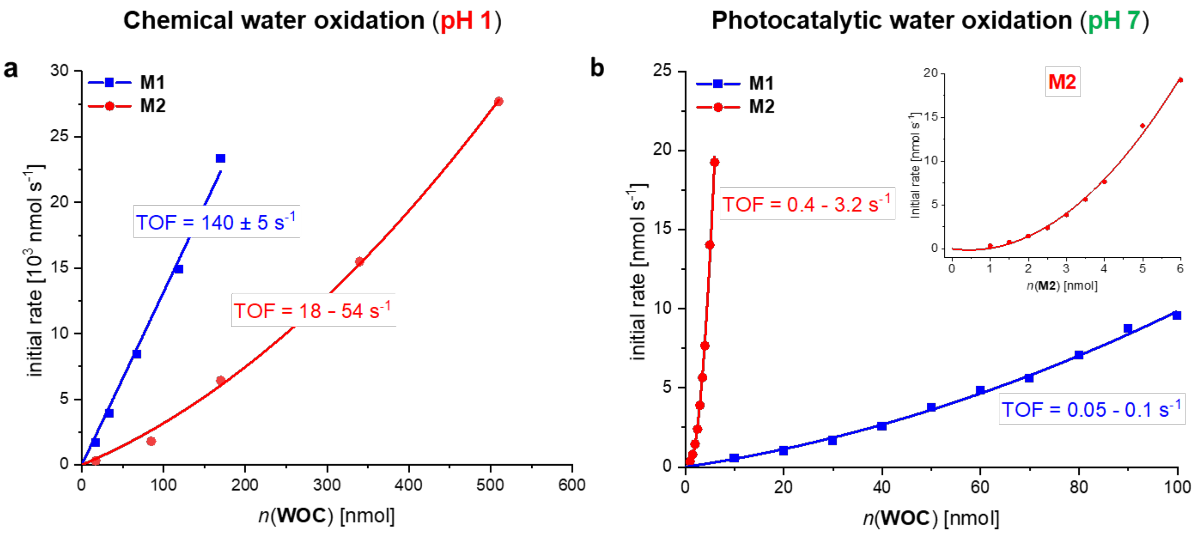

Fig. 2 | Chemical and photocatalytic water oxidation catalysis with M1 and M2. a, Chemical water oxidation catalysis with **M1** and **M2**: Plots of initial rates of O_2 evolution against the WOC concentration with corresponding linear (**M1**, blue) and quadratic (**M2**, red) regression fit (average TOF for **M1** was determined by linear regression, whereas range of individual TOFs is given for **M2**). Individual reaction rates were obtained by a linear fit of O_2 evolution curves for the first 2 s of catalysis for **M1** and **M2**, respectively; Experimental conditions: 4:6 CH_3CN/H_2O mixture using CAN as sacrificial oxidant (pH 1, triflic acid, *c*(CAN) = 0.6 M). **b**, Photocatalytic water oxidation catalysis with **M1** and **M2**: Plot of initial rates (obtained by linear fit of O_2 evolution curve between 50–60 s) of O_2 evolution against the WOC concentration and quadratic fit for second order kinetics**.** The observed second order dependency of **M2** is shown as inset. O_2 evolution experiments were performed at varying WOC concentrations in CH_3CN/H_2O 4:6 (pH 7, 50 mM phosphate buffer, c(PS) = 1.5 mM, c($Na_2S_2O_8$) = 37 mM).

pH-dependent NMR measurements. To probe for pH-dependent conformational changes in both **M1** and **M2** at the initial Ru^{II} state, ^1H NMR spectra were measured in aqueous 1:1 mixtures of D_2O (pD = 1.0 (0.1 M CF_3SO_3D) or pD = 7.0) and TFE-d_3 as a non-coordinating co-solvent for better solubility (Fig.

4). All signals were assigned to the individual protons based on 1D and 2D NMR spectroscopy (Supplementary Figs. 22–25). Both complexes display the anticipated planar symmetry as indicated by only one set of signals for all chemically nonequivalent protons. For **M1**, significant differences in the chemical shifts depending on the pD value were observed (Figs. 3a, b), which was especially evident for the *ortho* protons of the axial pyridines. While the blue-labelled *ortho* proton resonates at 8.19 ppm at pD 1.0, this signal is significantly upfield shifted to 6.39 ppm at pD 7.0. Conversely, reverse shifting is observed for the red-labelled *ortho* proton next to the bridging ligand. Whereas the upfield shifted protons are magnetically shielded due to proximity of the equatorial bda ligands,[50] the pronounced downfield shifts of the opposite *ortho*-protons indicate positioning above the open Ru site. At pD 7.0, severe signal broading was observed for both *ortho* protons, which was overcome by heating the sample to 333 K (Supplementary Fig. 24) and is attributed to the reduced structural flexibility of the ligand due to [C-H···N] hydrogen bonding interactions with the bda backbone. Further evidence for such stabilizing interactions is given by the pronounced downfield shift of the green-labelled bda proton compared to pD 1.0. In contrast, reference **M2** displayed pH-independent chemical shifts for all aromatic protons. Again, a significant difference in the chemical shifts of the *ortho* protons of the axial pyridines was observed, which indicates a different chemical environment due to a slight rotation of the axial pyridine units. While the red-labelled proton (8.56 ppm) is oriented more towards the open site of the catalytic center and is thus strongly deshielded, the blue-labelled proton (5.83 ppm) is again affected by the magnetic shielding of the nearby equatorial bda ligand (Fig. 3c and d). This conformation is further evidenced by a nuclear Overhauser effect (NOE) cross signal (Supplementary Fig. 25d) between the bda unit (yellow proton) and the axial biphenyl unit (purple proton). However, the three sharp signals for the bda ligand without any splitting at room temperature suggests fast switching of the axial ligand **L2** between the two symmetrical side-on conformations on the NMR time scale. Based on these data, we conclude that the conformation of **M1** is strongly affected by the proximal base in the ligand backbone. At pD 7.0, the bda unit is fixed inside the macrocyclic cavity by weak [C-H···N] interactions between the bda backbone and the free bipyridine base. Protonation of the proximal base[51] at pD 1.0 induces a ligand rotation due to electrostatic repulsion and now confines the active site in the cyclic cavity. ^{1}H NMR titration experiments from pD 1.0 to pD 7.0 for **M1** indicated the deprotonation followed by rotation of the bipyridine-containing ligand **L1** in the range of pD 1.0 to 4.0 (Supplementary Fig. 26) Therefore, the active Ru center is only fully confined in the macrocyclic cavity under highly acidic conditions at pD 1.0. For reference **M2**, weak [C-H···O] hydrogen bonding interactions between the axial and equatorial ligand spheres leads to a lateral orientation of the macrocyclic ligand over the whole pH range.

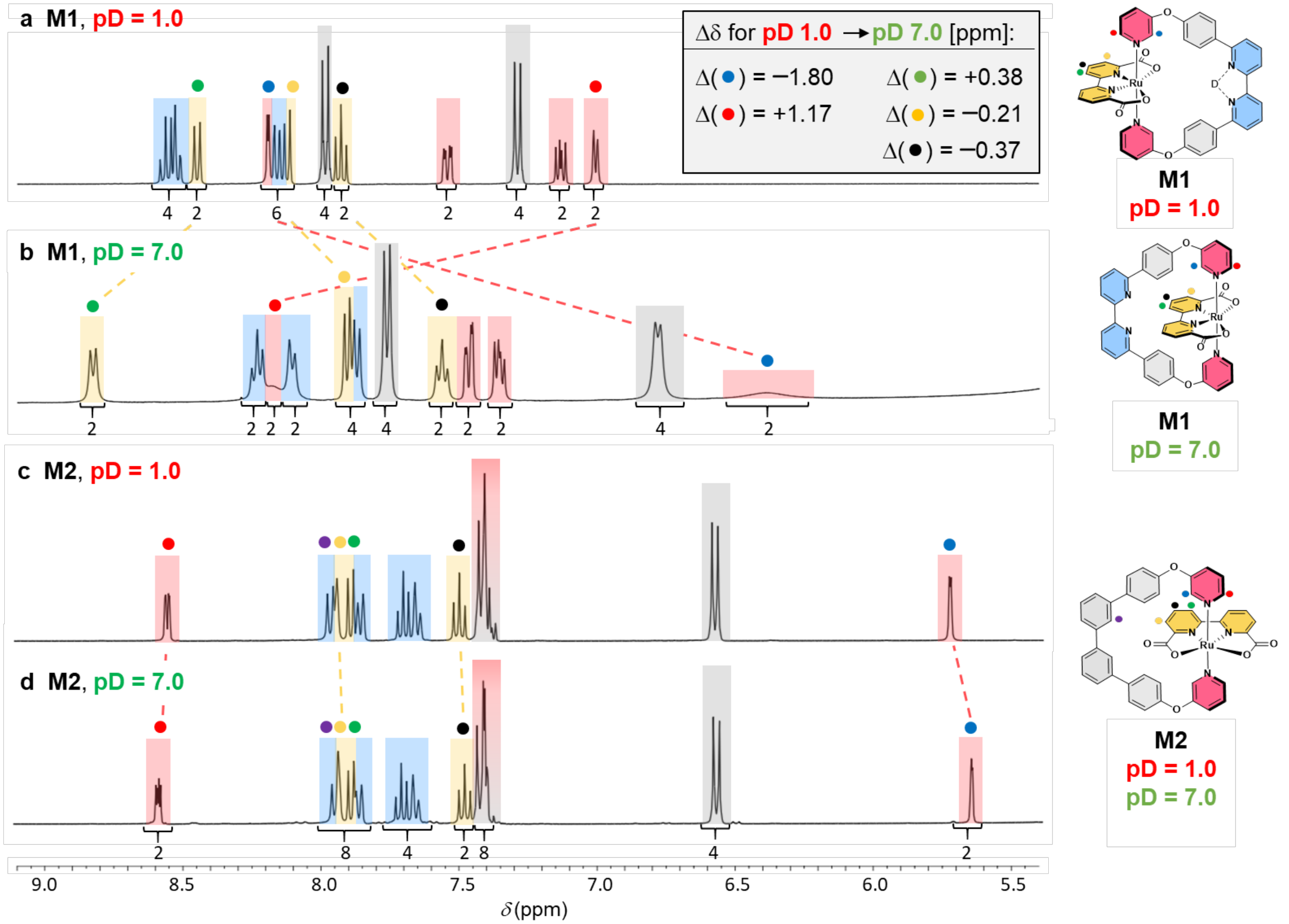

Fig. 3 | pD-dependent ^{1}H NMR experiments of M1 and M2. Aromatic region of the ^{1}H NMR spectra (1:1 TFE-d_3/D_2O, 400 MHz, ascorbic acid, rt) of complex **a**, **M1** at pD = 1.0 (0.1 M CF_3SO_3D), **b**, **M1** at pD = 7.0, **c**, **M2** at pD = 1.0 (0.1 M CF_3SO_3D), and **d**, **M2** at pD = 7.0 with the proposed molecular structure of the respective complex based on 2D-NMR structural analysis shown on the right (signals are color-coded in yellow (bda), red (axial pyridine), grey (biphenyl) or blue (bipyridine) as highlighted in the structure).

Single-crystal X-ray analysis. To gain a deeper insight into these conformational features, we grew single crystals of both **M1** and **M2** in the initial Ru^{II} state at neutral conditions and even of **M1** after acidic catalytic water oxidation. The ORTEP representations for all three solid-state structures in Fig. 4 (for crystallographic details Single crystal X-ray analysis in the Methods, Supplementary Note 4 and Supplementary Tables 5 and 6) unequivocally confirm the cyclic nature of the mononuclear complexes **M1** and **M2**, but each feature a different spatial orientation of the axial pyridine ligands. Remarkably, all three solid-state structures are in excellent agreement with the proposed predominant conformations derived from ^{1}H-NMR measurements for the macrocycles in solution. Under neutral conditions, both **M1** and **M2** exhibit a six-coordinated Ru atom with a distorted octahedral coordination geometry and two slightly different conformers are present in the unit cell of **M1**. The obtuse O-Ru-O angles of 121.8(1)°/122.7(1)° and 123.1(9)° for **M1** and **M2**, respectively, are comparable to the previously reported acyclic mononuclear complex [Ru(bda)(pic)$_2$] (122.9(9)°).[22] Structurally, the bridging macrocycle of **M1** is fixed over the bda backbone by weak [C-H···N] hydrogen bonding interactions[52] between the axial and equatorial ligand framework (Fig. 4b, 2.58(7) and 2.80(2) Å; Supplementary Fig. 28, 2.65(2) and 2.99(7) Å). This rigid conformation with torsional angles of 79.5° or 82.8° (55.8° and 82.5°) for the pyridine units relative to the open coordination site of the Ru center (Supplementary Fig. 27a,b) induces a slight deviation from an ideal linear orientation with a decreased N_{ax}-Ru-N_{ax} bond angle of 171.4(2)°/173.2(1)°. In contrast, reference **M2** shows a substantially different conformation for the bridging ligand and a more linear orientation of the axial pyridine units with a larger N_{ax}-Ru-N_{ax} bond angle of 175.5(4)°. Weak [C-H···O] hydrogen bonding interactions between the biphenyl backbone and one carboxylate of the equatorial bda ligand (Fig. 4a, 2.74(3) and 2.89(9) Å)[52] induce a lateral orientation of the macrocyclic ligand. This results in a smaller torsional twist of the axial pyridine units relative to the open coordination site of the Ru center with 10.0° and 37.9°, respectively (Supplementary Fig. 27c and Supplementary Table 4).

Searching for a structural model for **M1** after acidic catalytic water oxidation, we attempted to isolate catalytic intermediates directly from the reaction mixture after several catalytic turnovers by precipitation with NH_4PF_6. To our delight, orange needle-like single crystals suitable for X-ray analysis could be grown at room temperature during the precipitation process. To begin with, the Ru oxidation state of the isolated crystals was investigated by means of HR-MS measurements (Supplementary Fig. 31). Two species were observed by ESI-TOF experiments and the major component was assigned to the $[Ru^{III}(bda)(\mathbf{L1})]^+(PF_6)$ intermediate. In contrast, the *m/z* ratio for the second signal with ca. 10% relative intensity fits exactly to $[Ru^{IV}(bda)(\mathbf{L2})(OH)]^+(PF_6)$, which is in accordance to the respective Ru(IV) intermediate of complex **M1**. The assumed mixed Ru^{III}/Ru^{IV} oxidation state is further supported by an ^{1}H-NMR spectrum (Supplementary Fig. 32) that displayed the expected equilibrium between one set of broad signals and another set of clearly resolved signals corresponding to the paramagnetic Ru^{III} and diamagnetic Ru^{IV} species, respectively (Supplementary Figs. 33 and 34).

Compared to the ^{1}H NMR spectra of **M1** at the initial Ru^{II} state, the higher oxidation of the Ru center induces a significant downfield shift of the equatorial bda signals.[22] Therefore, we conclude that these crystals of **M1** obtained after acidic catalytic water oxidation represent the catalytic resting state at the

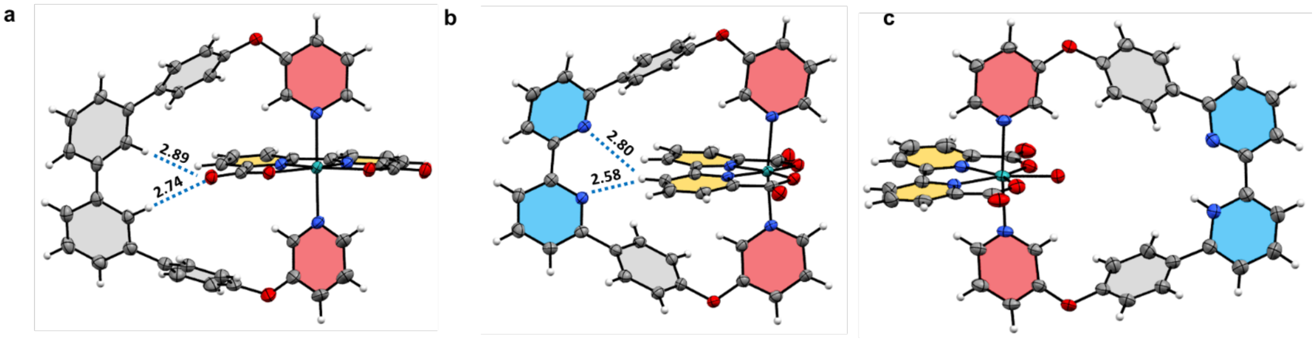

M2

M1

[(M1+H)(H_2O)]$^{2+}$(PF_6)$_2$

Fig. 4 | Single-crystal X-ray structures for M1, M2 and [(M1+H)(H_2O)]$^{2+}$(PF_6)$_2$. a, **M2** ([Ru^{II}(bda)(**L2**)]) **b**, **M1** ([Ru^{II}(bda)(**L1**)]) and **c**, **M1** after acidic catalytic water oxidation ([Ru^{III}(bda)(**L1**–H)(H_2O)]$^{2+}$(PF_6^-)$_2$); for **M1**, only one of the two macocyclic complexes in the unit cell is shown; organic solvent molecules and PF_6^- counterions are omitted for clarity; ORTEP diagram with thermal ellipsoids set at 50% probability; grey = C, white = H, red = O, purple = N, turquoise = Ru.

early transition from Ru^{III} to Ru^{IV} oxidation state. For the sake of clarity, we assume the Ru^{III} oxidation state for the following discussion, but it cannot be excluded that a minor fraction of the complexes is already oxidized to Ru^{IV} as evidenced by NMR and MS measurements for the isolated crystals. An ORTEP representation for the crystal structure of [Ru^{III}(bda)(**L1**-H)(H_2O)]$^{2+}$(PF_6^-)$_2$ is displayed in Fig. 4c. It is composed of a seven-coordinated [Ru^{III}(bda)(**L1**-H)]$^{2+}$ cation with a directly 7th coordinated H_2O ligand in a highly distorted pentagonal bipyramidal configuration and a significant increase of the O-Ru-O bite angle from 121.8(1)° to 136.4(1)°. The additional H_2O ligand directly points towards the cavity defined by the macrocyclic bridge. To balance the overall charge, on average 2.4 PF_6^- counterions compensate for the two positive charges at the Ru center and the protonated bipyridine moiety and the presumed partial protonation of a substrate H_2O molecule under the experimental acidic conditions.

Within the macrocyclic cavity, a well-defined hydrogen-bonding network preorganizes up to four H_2O molecules between the protonated bipyridine site, the Ru center, and the carboxylates of the equatorial bda ligand (Fig. 5). Intriguingly, three different occupancies give unprecedented insight into subtle equilibria at the coordination sphere for Ru(bda) at low oxidation states such as Ru^{II} and Ru^{III}.[23,53] In a minor occupancy (11.7%, Fig. 5a), three H_2O molecules are only loosely bound to the cavity. As a next step towards water oxidation, the first H_2O molecule approaches the Ru center ($d_{Ru–O}$ = 3.08 Å)[50] while being stabilized by two other H_2O molecules between the bipyridinium unit und the bda ligand as directional binding sites (22.1%, Fig. 5b). Finally, the main occupancy (66.2%, Fig. 5c) shows direct structural evidence for a 7th coordinated H_2O ligand in a distorted Ru^{III}(bda)-H_2O complex, which represents one of the key intermediates in the overall catalytic cycle. The short Ru–O distance of 2.06 Å indicates a strong affinity of the incoming H_2O ligand to the Ru center and is in perfect agreement with recent quantum-chemical calculations on $[Ru^{III}–OH_2]$ complexes in either approaching (d = 2.51 Å) or bonding mode (d = 2.07 Å).[54] This Ru^{III}(bda)-H_2O complex is again further stabilized by several preorganized water molecules within the cavity and a second 'ready-to-go' H_2O molecule, thus highly facilitating the subsequent nucleophilic attack at the catalytically active Ru^{V}=O oxidation state during the WNA pathway. Further experimental evidence for the proposed H_2O preorganization was obtained by an additional broad absorption at around 3620 cm^{-1} in the FT-IR spectrum of isolated crystals $[(\mathbf{M1}\text{-}H)(H_2O)]^{2+}(PF_6)_2$ (Supplementary Fig. 35). We attribute this band, which was not observed for similarly prepared samples of **M2**, to O-H stretching vibrations for H_2O molecules that strongly interact with the oxidized Ru center, as it was recently shown for a hydrogen-evolving catalyst.[55] Intriguingly, a similar absorption was also observed for a solution of **M1** only at pH 1, but not under neutral conditions (Supplementary Fig. 36). We therefore conclude that a defined water network within the cavity of **M1** under acidic conditions is not only formed and conserved in crystalline solids but also persists in solution phase. Reinvestigation of isolated crystals $[(\mathbf{M1}+H)(H_2O)]^{2+}(PF_6^{-})_2$ in chemical water oxidation resulted in virtually the same activity as for freshly prepared **M1** (Supplementary Fig. 37), once again demonstrating the high stability and activity of **M1**. Apparently, the crystal structure shown in Fig. 5 represents an active intermediate or resting state during the WOC cycle.

These results clearly highlight and justify our molecular design strategy towards a sophisticated second coordination sphere. Supramolecular preorganization of water molecules in a well-defined pocket around the catalytic Ru center resulted in high-performance molecular water oxidation catalysis and stabilized higher Ru^{III} or Ru^{IV} oxidation states. A Ru^{III} complex with a 7th coordinated H_2O ligand was isolated, which is typically rather short-lived due to violation of the 18-electron rule,[56] and unprecedented structural insight into early catalytic intermediates for the WNA pathway was obtained.

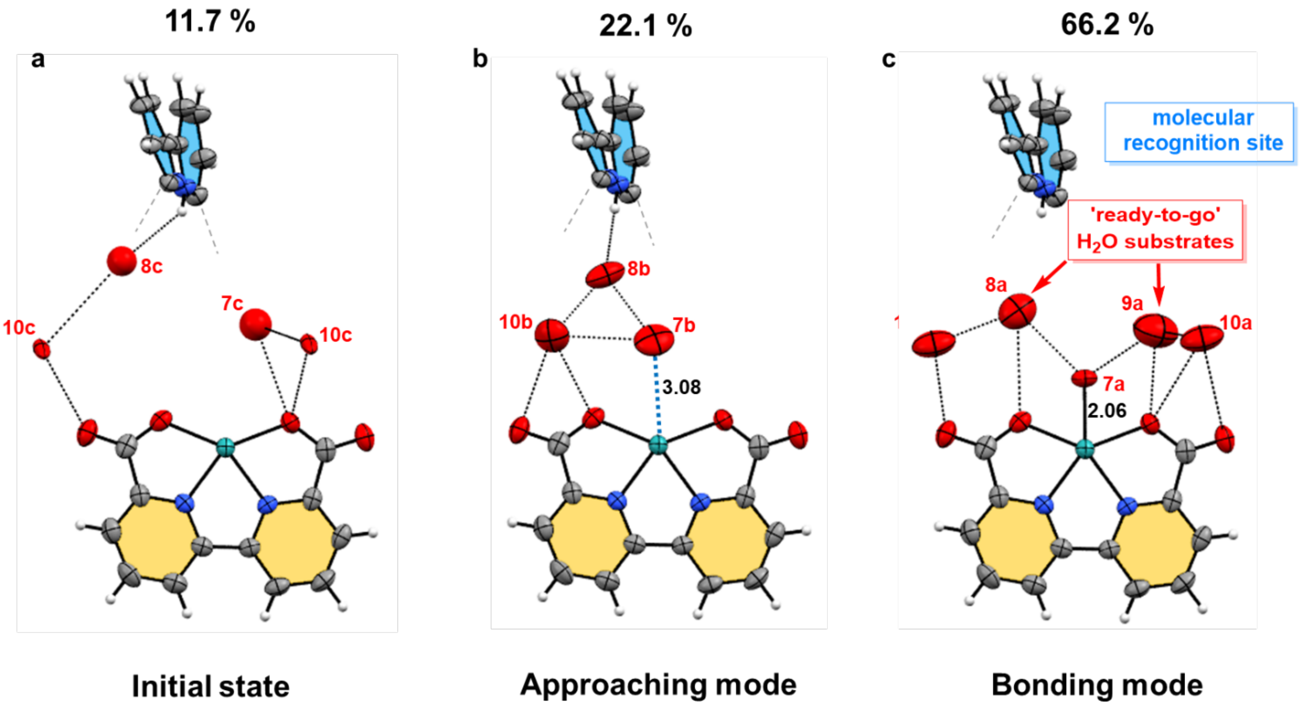

Fig. 5 | Three different states for the hydrogen-bonding network inside [(M1+H)(H_2O)]$^{2+}$(PF_6)$_2$. Three different states for the hydrogen-bonding network of preorganized H_2O molecules inside the supramolecular cavity of [(**M1**+H)(H_2O)]$^{2+}$(PF_6)$_2$ obtained by single-crystal X-ray analysis. **a**, Initial state (11.7% occupancy), **b**, approaching mode (22.1% occupancy) and **c**, bonding mode (66.2% occupancy) with additional H_2O substrates 'ready-to-go' for O–O bond formation via nucleophilic attack.

Proposed mechanisms for water oxidation with M1 and M2. After compiling all analytical data, we propose the following mechanistic picture for water oxidation with cyclic mononuclear Ru complexes (Fig. 6). For reference **M2** containing the unfunctionalized biphenyl unit, water oxidation always follows the bimolecular I2M mechanism independent of the applied experimental conditions. In accordance with the literature,[22–24] we propose a symmetrical bimolecular encounter complex for the rate-determining step (rds) of the I2M pathway for **M2**. The assumed lateral orientation of the macrocyclic ligand stabilizes this assembly by π-π interactions and facilitates the O–O bond formation via radical combination of two Ru^{V}=O intermediates (Fig. 6c). In contrast, the analogous bimolecular complex for **M1** at neutral conditions is sterically hindered by the presumed edge-to-edge orientation of the axial pyridine ligands, thus hampering the bimolecular approach, and significantly lowering the catalytic activity of **M**1 in the I2M mechanism at pH 7 (Fig. 6d). At pH 1 however, protonation of the proximal base in the ligand backbone induces a rotation of the macrocycle, which confines the active site in the cyclic cavity and impedes any bimolecular interactions at the active Ru site. This structural switch endowes **M1** obviously with an advantage compared to other mono- and dinuclear WOCs reported in literature that also involve a mechanistic switch from bimolecular I2M to monomolecular WNA mechanism.[57–59] For instance, a series of pocket-shaped Ru(bda) complexes equipped with flexible, aliphatic bridging ligands and structural similarity to **M1** and **M2** operate via a quite inefficent WNA mechanism.[50,60] For **M1** however, an X-ray structure for the predominant Ru^{III} resting state revealed that the well-defined macrocyclic pocket stabilizes the bound Ru^{III}-OH_2 center and preorganizes additional water molecules in close proximity. Thus, the kinetic barrier for the nucleophilic attack of a second H_2O molecule is strongly reduced, thus resulting in a mechanistic switch to the unimolecular WNA mechanism for **M1** under acidic conditions (Fig. 6b). Further evidence for this transition is provided by a change from secondary (1.2) to primary (1.6) KIE for **M1** under neutral and acidic conditions, respectively. Presumably, the enzyme-like nanoenvironment in the macrocyclic pocket for the active conformation of **M1** leads to a very product-like transition state, which explains the observed slightly lower KIE of 1.6 at pH 1.[61] Furthermore, this mechanistic switch and significantly enhanced catalytic performance of **M1** under acidic conditions are well reflected by a pronounced reduction of the overpotential from 440 to 290 mV when going from pH 7 to 1. In contrast, the overpotential for **M2** is much less affected by a change in pH (Supplementary Table 2 and Supplementary Figs. 4 and 5).

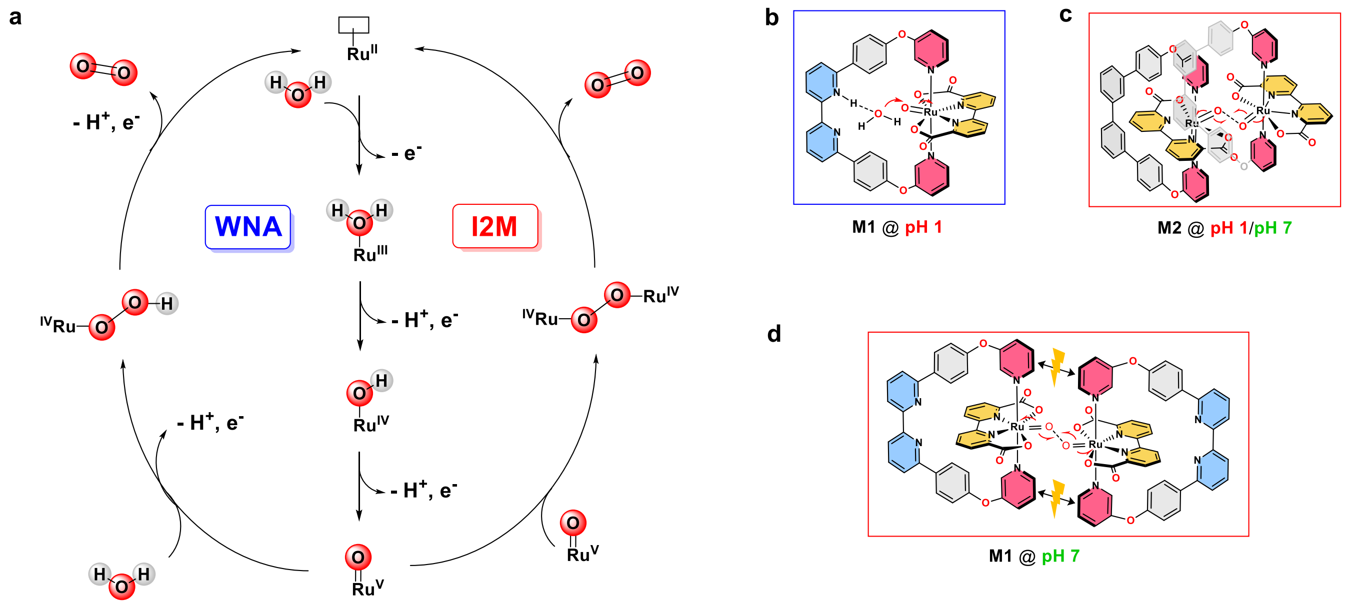

Fig. 6 | Mechanisms for water oxidation catalysis and proposed key intermediates for M1 and M2. a, Mechanistic picture for the water nucleophilic attack (WNA) and bimolecular radical-radical coupling (I2M) pathways of catalytic water oxidation. Graphical representation of the proposed key intermediates at the Ru^{V} state of the water oxidation cycle for **b**, **M1** at pH 1, **c**, **M2** at pH 1 and 7 and **d**, **M1** at pH 7.

Conclusions

In an enzyme-mimetic approach, we have synthesized the Ru(bda) catalyst **M1** whose catalytic activity is controlled by a bipyridine ligand located opposite to the metal centre in a macrocyclic architecture. In chemical water oxidation at pH 1, an impressive TOF of 140 ± 5 s^{-1} is achieved, which is far superior to the unsubstituted control compound **M2** (TOF = 18–54 s^{-1}) and even comparable to the natural archetype OEC-PSII. Detailed kinetic investigations disclosed a mechanistic switch from the bimolecular I2M mechanism for **M2** to the usually much less effective unimolecular WNA pathway for the base-containing **M1**. In this regard, single-crystal X-ray analysis for the Ru^{III} resting state of **M1** after catalytic water oxidation revealed the preorganization of several H_2O molecules within the rigid pocket around the active Ru center. Direct structural evidence for a 7th H_2O ligand directly coordinated to a catalytically active Ru^{III} species is observed, while further H_2O molecules are fixed as 'ready-to-go' substrates in proximity via hydrogen bonding to the protonated bipyridine site and carboxylates of the bda backbone. This well-defined H_2O network significantly reduces the kinetic barrier for this crucial and extremely effective nucleophilic attack and provides unprecedented insight into the initial states of O–O bond formation in the WNA mechanism. Under the neutral conditions for photocatalytic water oxidation however, weak [C-H···N] interactions between the bda backbone and the free bipyridine base induce a ligand rotation, which breaks the catalytic pocket and restricts any activity to an inferior and sterically hindered I2M mechanism. This study establishes a molecular design approach for water oxidation catalysis that conceptually mimics active sites in natural enzymes where water channels are pre-organized in molecular clefts similar to its natural counterpart. Whilst we demonstrated here the design of a catalytic pocket by pre-organizing the substrate water molecules from a ligand located opposite to the metal centre for accelerated O_2 evolution, we envision in a broader sense that our conceptual design will inspire many other kinds of catalytic transformations and might be efficiently implemented in solar fuel devices.

Methods

Synthesis towards molecular precursor 1. 4-(pyridin-3-yloxy)aniline (8.72 g, 46.8 mmol, 1.0 equiv.) was dissolved in 48 % aqueous HBr (60 mL) and a solution of $NaNO_2$ (6.78 g, 98.3 mmol, 2.1 equiv.) in H_2O (48 mL) was added dropwise over 10 min at 0 °C. After stirring for additional 2 h at room temperature, CuBr (10.1 g, 70.2 mmol, 1.5 equiv.) was added slowly at 0 °C and the mixture was stirred at room temperature for 2h and at 140 °C for 24 h. After cooling to room temperature, the crude product was carefully neutralized with saturated $NaHCO_3$ solution at 0 °C and extracted with ethyl acetate (3 x 50 mL). The combined organic phases were dried over anhydrous Na_2SO_4 and concentrated under reduced pressure. The residue was purified by flash chromatography (SiO_2, cyclohexane/ethyl acetate 60:10).

3-(4-bromophenoxy)pyridine. Yield: 6.60 g, 26.4 mmol (56%, Lit[62]: not reported). ^{1}H NMR (400 MHz, $CDCl_3$, rt): δ [ppm] = 8.40 (dd, $^{3}J_{H\text{-}H}$ = 5.1 Hz, , $^{4}J_{H\text{-}H}$ = 2.6 Hz, 2H, *H2* & *H6*), 7.50 – 7.45 (m, 2H, *H4* & *H5*), 7.32 – 7.28 (m, 2H, *H3'*), 6.93 – 6.89 (m, 2H, *H2'*). Analytic data are in accordance with the literature.[62]

A mixture of 3-(4-bromophenoxy)pyridine (1.05 g, 4.20 mmol, 1.0 equiv.), bis(pinacolato)diboron (2.35 g, 9.24 mmol, 2.2 equiv.) and KOAc (1.24 g, 12.6 mmol, 3.0 equiv.) in dry dioxane (5.3 mL) and dry DMF (0.7 mL) was degassed under nitrogen for 45 min. Subsequently, Pd(dppf)Cl_2 (92.2 mg, 126 µmol, 0.03 equiv.) was added and the mixture was stirred for 62 h at 95 °C. After cooling down to room temperature, the crude mixture was filtrated over celite and concentrated under reduced pressure. The residue was purified by flash chromatography (SiO_2, dichloromethane to dichloromethane / ethyl acetate 90:10).

3-(4-(4,4,5,5-tetramethyl-1,3,2-dioxaborolan-2-yl)phenoxy)pyridine (**1**). Yield: 766 mg, 2.58 mmol (61 %, Lit.[62]: not reported). ^{1}H NMR (400 MHz, $CDCl_3$, rt): δ [ppm] = 8.44 – 8.42 (m, 1H, *H2*), 8.39 (dd, $^{3}J_{H\text{-}H}$ = 4.5 Hz, $^{4}J_{H\text{-}H}$ = 1.6 Hz, 1H, *H6*), 7.83 – 7.79 (m, 2H, *H3'*), 7.33 – 7.27 (m, 2H, *H4* & *H5*), 7.02 – 6.98 (m, 2H, *H2'*), 1.35 (s, 12H). Analytic data are in accordance with the literature.[62]

Synthesis of bidentate ligands. A mixture of 6,6'-dibromo-2,2'-bipyridine (**BP1**) or 3,3'-dibromo-1,1'-biphenyl (**BP2**) (1.0 equiv.), 3-(4-(4,4,5,5-tetramethyl-1,3,2-dioxaborolan-2-yl)phenoxy) pyridine (**1**) (2.2 equiv.) and 2 M Na_2CO_3 aqueous solution (8.0 equiv.) in a mixture of toluene/ethanol (0.1 M, 4:1) was degassed under nitrogen by three consecutive freeze-pump-thaw cycles. Subsequently, $PdCl_2(PPh_3)_2$ (0.1 equiv.) was added and the resulting mixture was heated at 110 °C for 18 hours. After cooling down to room temperature, the solvent was removed under reduced pressure and the residue was diluted with dichloromethane. The organic phase was separated, and the aqueous phase extracted with dichloromethane (3×25 mL). The combined organic phases were dried over anhydrous Na_2SO_4 and concentrated under reduced pressure. The residue was purified by flash chromatography (SiO_2, cyclohexane/ethyl acetate 80:20 to 50:50).

6,6'-bis(4-(pyridin-3-yloxy)phenyl)-2,2'-bipyridine (**L1**). Yield: 324 mg, 655 µmol (82%). m.p. 182 °C. ^{1}H NMR (400 MHz, $CDCl_3$, rt): δ [ppm] = 8.57 (dd, ^{3}J = 7.8 Hz, ^{4}J = 0.9 Hz, 2H), 8.49 (dd, ^{4}J = 2.8, ^{5}J = 0.5 Hz, 2H), 8.41 (dd, ^{3}J = 4.6 Hz, ^{4}J = 1.4 Hz, 2H), 8.21 – 8.17 (m, 4H), 7.92 (t, ^{3}J = 7.8 Hz, 2H), 7.76 (dd, ^{3}J = 7.9 Hz, ^{4}J = 0.9 Hz, 2H), 7.38 (ddd, ^{3}J = 8.4 Hz, ^{4}J = 2.8, 1.5 Hz, 2H), 7.31 (ddd, ^{3}J = 8.4, 4.6 Hz, ^{5}J = 0.7 Hz, 2H), 7.19 – 7.15 (m, 4H). ^{13}C NMR (100 MHz, $CDCl_3$, rt) δ [ppm] = 157.5, 156.0, 155.6, 153.8, 144.8, 141.8, 137.9, 135.5, 128.9, 125.9, 124.3, 120.1, 119.5, 119.1. HRMS (ESI-TOF, pos. mode, MeCN/CHCl$_3$ 1:1): m/z calcd for $C_{32}H_{22}N_4O_2$+H$^+$: 495.1815 [M+H]$^+$; found: 495.1802. elemental analysis calcd. (%) for $C_{32}H_{22}N_4O_2$: C 77.72, H 4.48, N 11.33; found: C 77.54, H 4.63, N 11.38.

4,4'''-bis(pyridin-3-yloxy)-1,1':3',1'':3'',1'''-quaterphenyl (**L2**). Yield: 203 mg, 412 µmol (82%). ^{1}H NMR (400 MHz, CDCl$_3$, rt): δ [ppm] = 8.46 (d, ^{4}J = 2.6 Hz, 2H), 8.40 (d, ^{4}J = 3.9 Hz, 2H), 7.83 (t, ^{4}J = 1.7 Hz, 2H), 7.68 – 7.62 (m, 6H), 7.60 – 7.52 (m, 4H), 7.41 (ddd, ^{3}J = 8.4 Hz, ^{4}J = 2.7, 1.4 Hz, 2H), 7.34 (dd, ^{3}J = 8.4, 4.7 Hz, 2H), 7.15 – 7.10 (m, 4H). ^{13}C NMR (100 MHz, CDCl$_3$, rt) δ [ppm] = 155.9, 154.3, 143.7, 141.9, 141.0, 140.6, 137.5, 129.5, 129.1, 126.4, 126.4, 126.3, 126.2, 124.6, 119.5. HRMS (ESI-TOF, pos. mode, MeCN/CHCl$_3$ 1:1): m/z calcd for $C_{34}H_{24}N_2O_2$+Na$^+$: 515.1730 [M+Na]$^+$; found: 515.1730. elemental analysis calcd. (%) for $C_{34}H_{24}N_2O_2$: C 82.91, H 4.91, N 5.69; found: C 82.51, H 4.80, N 5.79.

Synthesis of mononuclear Ru complexes. [Ru(bda)(dmso)$_2$] (165 mg, 330 µmol, 1.1 equiv.) and the respective ligand (**L1**, **L2**) (300 µmol, 1.0 equiv.) were dissolved in a degassed mixture of chloroform (50 mL) and methanol (50 mL) and stirred for 14 hours at 65 °C under nitrogen. After cooling to room temperature, the solvent was removed under reduced pressure. The residue was purified by column chromatography (SiO$_2$, dichloromethane/methanol 10:0.5 to 10:3) and isolated as the first fraction.

[Ru(bda)(6,6'-bis(4-(pyridin-3-yloxy)phenyl)-2,2'-bipyridine)] (**M1**). Yield: 123 mg, 147 µmol (49 %). m.p. >300 °C. ^{1}H NMR (400 MHz, CD_2Cl_2/CD_3OD (1:1) + ascorbic acid, rt): δ [ppm] = 8.84 (dd, ^{3}J = 8.1 Hz, ^{4}J = 1.0 Hz, 2H), 8.65 (dd, ^{3}J = 5.3 Hz, ^{4}J = 1.3 Hz, 2H), 8.12 (t, ^{3}J = 7.8 Hz, 2H), 7.97 (dd, ^{3}J = 7.8 Hz, ^{4}J = 0.8 Hz, 2H), 7.79 – 7.77 (m, 4H), 7.69 – 7.64 (m, 4H), 7.43 – 7.32 (m, 6H), 6.61 – 6.55 (m, 4H), 5.59 (d, ^{4}J = 2.5 Hz, 2H). ^{13}C NMR (100 MHz, CD_2Cl_2/CD_3OD (1:1) + ascorbic acid, rt) δ [ppm] = 174.4, 159.8, 159.5, 159.1, 156.8, 156.4, 154.3, 150.1, 139.8, 138.9, 136.1, 132.2, 130.9, 127.8, 126.2, 121.9, 121.7, 121.7. UV/Vis (CH_3CN/H_2O 4:6 (pH 1)): λ_{max} (ε) = 254 (42283), 302 (39153), 345 (18765), 454 (4954), 482 nm (4766 M^{-1} cm^{-1}); (CH_3CN/H_2O 4:6 (pH 7)): λ_{max} (ε) = 253 (39909), 304 (31047), 366 (8854), 458 (4003), 482 nm (3537 M^{-1} cm^{-1}). HRMS (ESI-TOF, pos. mode, MeOH/CH_2Cl_2 1:1): m/z calcd for $C_{44}H_{28}N_6O_6Ru^+$: 838.1108 [M]$^+$; found: 838.1112. elemental analysis calcd. (%) for $C_{32}H_{22}N_4O_2$: C 63.08, H 3.37, N 10.03; found: C 62.79, H 3.50, N 10.00.

[Ru(bda)(4,4'''-bis(pyridin-3-yloxy)-1,1':3',1'':3'',1'''-quaterphenyl)] (**M2**). Yield: 87.8 mg, 105 µmol (35 %). m.p. >300 °C. ^{1}H NMR (400 MHz, CD_2Cl_2/CD_3OD (1:1) + ascorbic acid, rt): δ [ppm] = 8.29 (dd, ^3J = 8.5 Hz, ^4J = 5.4 Hz, 2H), 8.05 (m, 2H), 7.99 (dd, ^3J = 8.1 Hz, ^4J = 0.9 Hz, 2H), 7.91 (dd, ^3J = 7.7 Hz, ^4J = 0.9 Hz, 2H), 7.84 (dt, ^3J = 7.0 Hz, ^4J = 1.8 Hz, 2H), 7.69 – 7.63 (m, 4H), 7.58 (t, ^3J = 7.9 Hz, 2H), 7.50 – 7.47 (m, 4H), 7.42 (ddd, ^3J = 8.5 Hz, ^4J = 2.6 Hz, 1.1 Hz, 2H), 7.27 (dd, ^3J = 8.5 Hz, 5.6 Hz, 2H), 6.75 – 6.70 (m, 4H), 6.24 (d, ^4J = 2.0 Hz, 2H). ^{13}C NMR (100 MHz, CD_2Cl_2/CD_3OD (1:1) + ascorbic acid, rt)

δ [ppm] = 173.9, 160.2, 157.8, 156.5, 154.1, 149.2, 142.6, 142.5, 140.1, 137.3, 132.3, 131.0, 130.5, 130.3, 127.4, 126.9, 126.3, 126.1, 125.9, 124.4, 121.2. UV/Vis (CH_3CN/H_2O 4:6 (pH 1)): λ_{max} (ε) = 253 (66036), 303 (27017), 356 (10670), 460 (4123), 492 nm (4052 M^{-1} cm^{-1}); (CH_3CN/H_2O 4:6 (pH 7)): λ_{max} (ε) = 254 (63988), 306 (24275), 358 (9988), 458 (4003), 492 nm (3454 M^{-1} cm^{-1}). HRMS (ESI-TOF, pos. mode, $MeOH/CH_2Cl_2$ 1:1): *m/z* calcd for $C_{46}H_{30}N_4O_6Ru^+$: 836.1209 $[M]^+$; found: 836.1233. elemental analysis calcd. (%) for $C_{32}H_{22}N_4O_2$: C 66.10, H 3.62, N 6.70; found: C 65.63, H 3.69, N 6.73.

Single crystal X-ray analysis. Single crystals of **M1** or **M2** were obtained by slow diffusion of diethyl ether in either a $CHCl_3$/MeOH (1:1) or DCM/MeOH (1:1) solution of the complexes **M1** and **M2**, respectively, which were stored in a refrigerator at 5 °C. Single crystals for complex $[(\mathbf{M1}\text{-H})(H_2O)]^{2+}(PF_6^-)_2$ were obtained following a recent literature report for the crystallization of Ru(bda) complexes after chemical water oxidation conditions:[22] Complex **M1** (10 mg, 12 µmol) was dissolved in 4 mL CH_3CN/H_2O 4:6 (pH 1, triflic acid) and cerium ammonium nitrate (400 mg, 720 µmol; ~60 eq.) was added stepwise. After vigorous oxygen evolution, subsequent addition of excess NH_4PF_6 led to slow precipitation and crystal formation after storing the mixture for several days in a refrigerator at 5 °C. Single crystal X-ray diffraction data were collected at 100 K on a Bruker D8 Quest Kappa Diffractometer with a PhotonII CPAD area detector and multi-layered mirror monochromated Cu Kα radiation (λ = 1.54178 Å). The structures were solved using direct methods, expanded with Fourier techniques and refined with the SHELX software package.[63] All non-hydrogen atoms were refined anisotropically. Hydrogen atoms were assigned to geometrically idealized positions and were included in calculation of structure factors. For all crystal structures, residual electron density for solvent molecules could not be modelled satisfactorily. Therefore, the PLATON squeeze routine was applied to remove the respective electron density.[64,65] The remaining structure could then be refined nicely.

Chemical water oxidation. The measurements were performed with a standardized procedure as described in our previous publications.[25,66–68] Water oxidation experiments under chemical conditions were carried out under ambient conditions in reaction vessels (*V* = 20.6 mL) connected to pressure sensors (Honeywell, SSCDANN030PAAA5, absolute pressure, 0 to 30 psi). For every experiment, CAN (1.0 g, 1.82 mmol) was dissolved in acetonitrile/water 4:6 mixture (3.0 mL, pH 1, triflic acid) and the catalyst solution (400 µL stock solution) was then injected through a septum using a Hamilton syringe. Via gas chromatography (Shimadzu GC-2010 Plus, thermal conductivity detector at 30 mA, argon as carrier gas), the gas composition of the head space after each catalytic experiment (500 µL) was determined. The catalytic stability is defined by the respective turnover number (TON), which was calculated by dividing the total amount of generated oxygen by the amount of used catalyst. The amount of generated oxygen was determined by applying the ideal gas law: $\Delta p \times V = \Delta n \times R \times T$ (T = 293.15 K, V = 20.6 mL, R = 8.314 J K^{-1} mol^{-1}). For each concentration, a TON was calculated and the highest TON is given. The catalytic activity of molecular catalysts was determined by the turnover frequency (TOF). Therefore, the initial rate of catalysis for each concentration was calculated via linear regression of the first two seconds of catalysis. In case of a linear dependency between the respective initial rates and the catalyst concentration, the slope of the linear regression represents the averaged TOF. A range of the observed TOF values, calculated for each concentration, is given when a quadratic dependency is observed.

Photocatalytic water oxidation. The measurements were performed in an Oxygraph Plus Clark-electrode system with a transparent reaction chamber (Hansatech Instruments Ltd.) at 20 °C following a standardized procedure as described in our previous publications.[25,67,68] A Clark electrode was used for oxygen detection. The samples were irradiated using a 150 W xenon lamp (Newport) equipped with a 400 nm cutoff filter. All the experiments were carried out under a light intensity of 100 mW cm^{-1}, which was calibrated by using CCS 200/M wide range spectrometer (Thorlabs) in combination with a PM 200 optical power meter equipped with a S121C sensor (Thorlabs), which was installed in a modified oxygen chamber (Hansatech Instruments Ltd.). Before the experiments, a stock solution of photosensitizer (PS) $[Ru(bpy)_3]Cl_2$ ($c([Ru(bpy)_3]Cl_2)$ = 1.5 mM) and $Na_2S_2O_8$ ($c(Na_2S_2O_8)$ = 37 mM) as sacrificial electron acceptor (SEA) in CH_3CN/H_2O 4:6 mixtures (pH 7, 50 mM phosphate buffer) was prepared in the dark. At a constant temperature of 20 °C, the reaction chamber was filled with an aliquot of this solution (1.5 mL), mixed with catalyst solution at various concentrations (total volume: 2 mL) and kept in the dark for additional 50 s prior to irradiation. For each concentration, a TON was calculated (maximum amount of evolved oxygen during catalysis divided by the amount of used catalyst) and the highest TON is reported. After an initial induction period of ~1 s, the TOF for each concentration was determined based on the initial rate of catalysis. Therefore, the oxygen evolution curve was plotted against the reaction time and the initial rate was extracted by linear regression analysis of the oxygen evolution amount versus the time for the first five to ten seconds of catalysis. The averaged TOF was then determined from the slope of a linear regression of the initial rates of each concentration *vs*. the respective catalyst amount. In case of a quadratic dependency, a range of the observed TOF values, calculated for each concentration, is given.

Kinetic Isotope Experiments. Based on standardized procedures described in our previous publications,[25,66–68] the experiments were performed using a Oxygraph Plus Clark-electrode system (Hansatech Instruments Ltd.) for oxygen detection at a constant temperature of 20 °C. If the relative reactions rates for non-deuterated and deuterated solvent differ by approximately a factor of two, the reaction is characterized by a primary deuterium kinetic isotope effect (KIE) and a direct O-H/D bond cleavage is involved in the rate-determining step (rds) of the water nucleophilic attack pathway.[61] In contrast, for the bimolecular I2M mechanism no direct hydrogen substitution takes place and thus a secondary kinetic isotope effect (KIE = 0.7 – 1.5) is observed.[61] The experiments under conditions of chemical water oxidation were performed in 2.0 mL of a 4:6 acetonitrile/water (H_2O or D_2O (99.9 % purity), pH 1, acid: triflic acid) mixture in the presence of CAN (c = 0.525 M) as sacrificial electron acceptor. For each measurement, 1.5 mL of a freshly prepared CAN solution (*c* = 0.7 M, 4:6 acetonitrile/water (H_2O or D_2O, pH 1)) was transferred to the transparent reaction chamber and after the baseline was constant (~ 40 s), 0.5 mL of the catalyst solution at varying concentrations was added. The experiments under photocatalytic conditions were performed in accordance with the procedures described for photocatalytic water oxidation. Therefore a stock solution of PS ($c([Ru(bpy)_3]Cl_2)$ = 1.5 mM) and SEA ($c(Na_2S_2O_8)$ = 37 mM) in 4:6 acetonitrile/water (H_2O or D_2O (99.9 % purity); pH 7, 50 mM phosphate buffer) was prepared in the dark. An aliquot of this solution (1.5 mL) was then mixed with a varying amount of catalyst concentration (total volume: 2 mL) in the dark. Irradiation was started at 50 s to allow thermal equilibration of the sample at a constant temperature of 20 °C. The reaction rates in H_2O ($k(H_2O)$) and D_2O ($k(D_2O)$) were calculated by determining the initial rate of catalysis for each concentration (linear regression of the oxygen evolution curve during the first five to ten seconds of reaction).

Stability test. To investigate the stability of the respective catalyst after chemical water oxidation, each complex (10.0 mg, 3.0 µmol) was dissolved in a mixture of CH_3CN/H_2O 4:6 (1.0 mL, pH 1, triflic acid). After addition of sacrificial oxidant CAN (500 mg, 960 µmol), intensive oxygen evolution occurred (~40 catalytic cycles). Then, ammonium hexafluorophosphate (250 mg) was added and a brown precipitate was formed, which was filtered off, washed with water, and dried under reduced pressure. The sample was redissolved, reduced with ascorbic acid and analysed by MALDI TOF mass spectrometry (positive, *trans*-2-[3-(4-tert-butylphenyl)-2-methyl-2-propenylidene] (DCTB), CH_2Cl_2/CH_3OH 1:1).

Data availability

Crystallographic data for the structures reported in this Article have been deposited at the Cambridge Crystallographic Data Centre under deposition numbers CCDC 2157734 (**M1**), 2157733 (**M2**) and 2157735 ([(**M1**-H)(H_2O)]$^{2+}$(PF_6)$_2$). Copies of the data can be obtained free of charge from www.ccdc.cam.ac.uk/structures/. All other source data is available from the authors upon reasonable request.

Acknowledgements

This project has received funding from the European Research Council (ERC) under the European Union's Horizon 2020 Research and Innovation Program (grant agreement No. 787937). The authors thank Maximilian Roth for synthetic support and Dr. Kazutaka Shoyama for valuable discussions on X-ray crystallography.

Author Contributions

F.W. initiated the project and supervised it together with F.B.. N.N. performed all experiments including the synthesis, NMR studies, the characterization of the catalytic properties and the growth of the single crystals for crystallographic analysis. A.-M.K. conducted the crystallographic measurements and analysis. All authors contributed to writing the manuscript.

Competing interest

The authors declare no competing interests.

References

1 Lehn, J.-M. Supramolecular Chemistry. *Science* **260**, 1762–1763 (1993).

2 Raynal, M., Ballester, P., Vidal-Ferran, A., van Leeuwen, P. W. N. M. Supramolecular catalysis. Part 2: artificial enzyme mimics. *Chem. Soc. Rev.* **43**, 1734–1787 (2014).

3 Fischer, E. Einfluss der Configuration auf die Wirkung der Enzyme. *Ber. Dtsch. Chem. Ges.* **27**, 3479–3483 (1894).

4. Dydio, P., Reek, J. N. H. Supramolecular control of selectivity in transition-metal catalysis through substrate preorganization. *Chem. Sci.* **5**, 2135–2145 (2014).

5. Brown, C. J., Toste, F. D., Bergman, R. G., Raymond, K. N. Supramolecular Catalysis in Metal–Ligand Cluster Hosts. *Chem. Rev.* **115**, 3012–3035 (2015).

6. Zarra, S., Wood, D. M., Roberts, D. A., Nitschke, J. R. Molecular containers in complex chemical systems. *Chem. Soc. Rev.* **44**, 419–432 (2015).

7. Mulder, D. W. et al. Stepwise [FeFe]-hydrogenase H-cluster assembly revealed in the structure of HydA$^{\Delta EFG}$. *Nature* **465**, 248–251 (2010).

8. Lubitz, W., Ogata, H., Rüdiger, O., Reijerse, E. Hydrogenases. *Chem. Rev.* **114**, 4081–4148 (2014).

9. Supekar, S., Gamiz-Hernandez, A. P., Kaila, V. R. I. A Protonated Water Cluster as a Transient Proton-Loading Site in Cytochrome *c* Oxidase. *Angew. Chem. Int. Ed.* **55**, 11940–11944 (2016).

10. Wikström, M., Krab, K., Sharma, V. Oxygen Activation and Energy Conservation by Cytochrome *c* Oxidase. *Chem. Rev.* **118**, 2469–2490 (2018).

11. Umena, Y., Kawakami, K., Shen, J.-R., Kamiya, N. Crystal structure of oxygen-evolving photosystem II at a resolution of 1.9 Å. *Nature* **473**, 55–60 (2011).

12. Cox, N., Pantazis, D. A., Neese, F., Lubitz, W. Biological Water Oxidation. *Acc. Chem. Res.* **46**, 1588–1596 (2013).

13. Suga, M. et al. An oxyl/oxo mechanism for oxygen-oxygen coupling in PSII revealed by an x-ray free-electron laser. *Science* **366**, 334–338 (2019).

14. Ringe, D., Petsko, G. A. How Enzymes Work. *Science* **320**, 1428–1429 (2008).

15. Hammarström, L., Styring, S. Proton-coupled electron transfer of tyrosines in Photosystem II and model systems for artificial photosynthesis: the role of a redox-active link between catalyst and photosensitizer. *Energy Environ. Sci.* **4**, 2379–2388 (2011).

16. Kanady, J. S., Tsui, E. Y., Day, M. W., Agapie, T. A. Synthetic Model of the Mn_3Ca Subsite of the Oxygen-Evolving Complex in Photosystem II. *Science* **333**, 733–736 (2011).

17. Zhang, C., Chen, C., Dong, H., Shen, J.-R., Dau, H., Zhao, J. A synthetic Mn_4Ca-cluster mimicking the oxygen-evolving center of photosynthesis. *Science* **348**, 690–693 (2015).

18. Kärkäs, M. D., Verho, O., Johnston, E. V., Åkermark, B. Artificial Photosynthesis: Molecular Systems for Catalytic Water Oxidation. *Chem. Rev.* **114**, 11863–12001 (2014).

19. Blakemore, J. D., Crabtree, R. H., Brudvig, G. W. Molecular Catalysts for Water Oxidation. *Chem. Rev.* **115**, 12974–13005 (2015).

20. Hessels, J., Detz, R. J., Koper, M. T. M., Reek, J. N. H. Rational Design Rules for Molecular Water Oxidation Catalysts based on Scaling Relationships. *Chem. Eur. J.* **23**, 16413–16418 (2017).

21. Gersten, S. W., Samuels, G. J., Meyer, T. J. Catalytic oxidation of water by an oxo-bridged ruthenium dimer. *J. Am. Chem. Soc.* **104**, 4029–30 (1982).

22. Duan, L., Fischer, A., Xu, Y., Sun, L. Isolated Seven-Coordinate Ru(IV) Dimer Complex with $[HOHOH]^-$ Bridging Ligand as an Intermediate for Catalytic Water Oxidation. *J. Am. Chem. Soc.* **131**, 10397–10399 (2009).

23. Zhang, B., Sun, L. Ru-bda: Unique Molecular Water-Oxidation Catalysts with Distortion Induced Open Site and Negatively Charged Ligands. *J. Am. Chem. Soc.* **141**, 5565–5580 (2019).

24. Duan, L. et al. A molecular ruthenium catalyst with water-oxidation activity comparable to that of photosystem II. *Nat. Chem.* **4**, 418–423 (2012).

25. Schulze, M., Kunz, V., Frischmann, P. D., Würthner, F. A supramolecular ruthenium macrocycle with high catalytic activity for water oxidation that mechanistically mimics photosystem II. *Nat. Chem.* **8**, 576–583 (2016).

26. Shaffer, D. W., Xie, Y., Concepcion, J. J. O–O bond formation in ruthenium-catalyzed water oxidation: single-site nucleophilic attack vs. O–O radical coupling. *Chem. Soc. Rev.* **46**, 6170–6193 (2017).

27. Kunz, V., Schmidt, D., Röhr, M. I. S., Mitrić, R., Würthner, F. Supramolecular Approaches to Improve the Performance of Ruthenium-Based Water Oxidation Catalysts. *Adv. Energy Mater.* **7**, 1602939 (2017).

28. Matheu, R., Ertem, M. Z., Gimbert-Suriñach, C., Sala, X., Llobet, A. Seven Coordinated Molecular Ruthenium–Water Oxidation Catalysts: A Coordination Chemistry Journey. *Chem. Rev.* **119**, 3453–3471 (2019).

29. Helm, M. L., Stewart, M. P., Bullock, R. M., DuBois, M. R., DuBois, D. L. A Synthetic Nickel Electrocatalyst with a Turnover Frequency Above 100,000 s^{-1} for H_2 Production. *Science* **333**, 863–866 (2011).

30. Song, N. et al. Base-enhanced catalytic water oxidation by a carboxylate–bipyridine Ru(II) complex. *Proc. Natl Acad. Sci. USA* **112**, 4935–4940 (2015).

31. Matheu, R. et al. Intramolecular Proton Transfer Boosts Water Oxidation Catalyzed by a Ru Complex. *J. Am. Chem. Soc.* **137**, 10786–10795 (2015).

32. Xie, Y., Shaffer, D. W., Lewandowska-Andralojc, A., Szalda, D. J., Concepcion, J. J. Water Oxidation by Ruthenium Complexes Incorporating Multifunctional Bipyridyl Diphosphonate Ligands. *Angew. Chem. Int. Ed.* **55**, 8067–8071 (2016).

33. Li, B. et al. Oxygen evolution from water oxidation on molecular catalysts confined in the nanocages of mesoporous silica. *Energy Environ. Sci.* **5**, 8229–8233 (2012).

34. Yu, F. et al. Control over Electrochemical Water Oxidation Catalysis by Preorganization of Molecular Ruthenium Catalysts in Self-Assembled Nanospheres. *Angew. Chem. Int. Ed.* **57**, 11247–11251 (2018).

35. Zaffaroni, R., Orth, N., Ivanović-Burmazović, I., Reek, J. N. H. Hydrogenase Mimis in $M_{12}L_{24}$ Nanospheres to Control Overpotential and Activity in Proton-Reduction Catalysis. *Angew. Chem. Int. Ed.* **59**, 18485–18489 (2020).

36. Brezinksi, W. P. et al. [FeFe]-Hydrogenase Mimetic Metallopolymers with Enhanced Catalytic Acitvity for Hydrogen Production in Water. *Angew. Chem. Int. Ed.* **57**, 11898–11902 (2018).

37. Daubignard, J., Detz, R. J., Jans, A. C. H., de Bruin, B., Reek, J. N. H. Rational Optimization of Supramolecular Catalysts for the Rhodium-Catalyzed Assymmetric Hydrogenation Reaction. *Angew. Chem. Int. Ed.* **56**, 13056–13060 (2017).

38. Wen, J., Wang, F., Zhang, X. Asymmetric hydrogenation catalyzed by first-row transition metal complexes. *Chem. Soc. Rev.* **50**, 3211–3237 (2021).

39. Fang, W., Breit, B. Tandem Regioselective Hydroformylation-Hydrogenation of Internal Alkynes Using a Supramolecular Catalyst. *Angew. Chem. Int. Ed.* **57**, 14817–14821 (2018).

40. Nurttila, S. S., Linnebank, P. R., Krachko, T., Reek, J. N. H. Supramolecular Approaches to Control Activity and Selectivity in Hydroformylation Catalysis. *ACS Catal.* **8**, 3469–3488 (2018).

41. Das, S., Incarvito, C. D., Crabtree, R. H., Brudvig, G. W. Molecular Recognition in the Selective Oxygenation of Saturated C–H Bonds by a Dimanganese Catalyst. *Science*, **312**, 1941–1943 (2006).

42. Kuninobu, Y., Ida, H., Nishi, M., Kanai, M. A meta-selective C–H borylation directed by a secondary interaction between ligand and substrate. *Nat. Chem.* **7**, 712–717 (2015).

43. Fanourakis, A., Docherty, P. J., Chuentragool, P., Phipps, R. J. Recent Developments in Enantioselective Transition Metal Catalysis Featuring Attractive Noncovalent Interactions between Ligand and Substrate. *ACS Catal.* **10**, 10672–10714 (2020).

44. Schwarzer, M. C., Fujioka, A., Ishii, T., Ohmiya, H., Mori, S., Sawamura, M. Enantiocontrol by assembled attractive interactions in copper-catalyzed asymmetric direct alkynylation of α-ketoesters with terminal alkynes: OH···O/sp^3-CH···O two-point hydrogen bonding combined with dispersive attractions. *Chem. Sci.* **9**, 3484–3493 (2018).

45. Frost, J. R., Huber, S. M., Breitenlechner, S., Bannwarth, C., Bach, T. Enantiotopos-Selective C–H Oxygenation Catalyzed by a Supramolecular Ruthenium Complex. *Angew. Chem. Int. Ed.* **54**, 691–695 (2015).

46. Vicens, L., Olivo, G., Costas, M. Remote Amino Acid Recognition Enables Effective Hydrogen Peroxide Activation at a Manganese Oxidation Catalyst. *Angew. Chem. Int. Ed.* **61**, e202114932 (2022).

47. Dydio, P., Detz, R. J., Reek, J. N. H. Precise Supramolecular Control of Selectivity in the Rh-Catalyzed Hydroformylation of Terminal and Internal Alkenes. *J. Am. Chem. Soc.* **135**, 10817–10828 (2013).

48. Parent, A. R., Crabtree, R. H., Brudvig, G. W. Comparison of primary oxidants for water-oxidation catalysis. *Chem. Soc. Rev.* **42**, 2247–2252 (2013).

49. Limburg, B., Bouwman, E., Bonnet, S. Rate and Stability of Photocatalytic Water Oxidation using $[Ru(bpy)_3]^{2+}$ as Photosensitizer. *ACS Catal.* **6**, 5273–5284 (2016).

50. Liu, T. et al. Isolation and Identification of Pseudo Seven-Coordinate Ru(III) Intermediate Completing the Catalytic Cycle of Ru-bda Type of Water Oxidation Catalysts. *CCS Chem.* **4**, 2481–2490 (2022).

51. Liu, Z., Gao, Y., Wang, J., Yao, Y. N., Wei, Y., Chen, X. Protonation effect on catalytic water oxidation activity of a mononuclear Ru catalyst containing a free pyridine unit. *J. Energy Chem.* **27**, 1402-1408 (2018).

52. Steiner, T. The Hydrogen Bond in the Solid State. *Angew. Chem. Int. Ed.* **41**, 48-76 (2002).

53. Matheu, R. et al. Behavior of Ru–bda Water-Oxidation Catalysts in Low Oxidation States. *Chem. Eur. J.* **24**, 12838–12847 (2018).

54. Daniel, Q. et. al. Rearranging from 6- to 7-coordination initiates the catalytic activity: An EPR study on a Ru-bda water oxidation catalyst. *Coord. Chem. Rev.* **346**, 206–215 (2017).

55. Li, X. et al. Introducing Water-Network-Assisted Proton Transfer for Boosted Electrocatalytic Hydrogen Evolution with Cobalt Corrole. *Angew. Chem. Int. Ed.* **61**, e202114310 (2022).

56. Pyykkö, P. Understanding the eighteen-electron rule. *J. Organomet. Chem.* **691**, 4336–4340 (2006).

57. Tong, L., Duan, L., Xu, Y., Privalov, T., Sun., L. Structural Modifications of Mononuclear Ruthenium Complexes: A Combined Experimental and Theoretical Study on the Kinetics of Ruthenium-Catalyzed Water Oxidation. *Angew. Chem. Int. Ed.* **50**, 445–449 (2011).

58. Staehle, R. et al. Water Oxidation Catalyzed by Mononuclear Ruthenium Complexes with a 2,2’-Bipyridine-6,6’-dicarboxylate (bda) Ligand: How Ligand Environment Influences the Catalytic Behavior. *Inorg. Chem.* **53**, 1307–1319 (2014).

59. Liu, Z., Gao, Y., Zhang, M., Liu, J. Design of a dinuclear ruthenium based catalyst with a rigid xanthene bridge for catalytic water oxidation. *Inorg. Chem. Commun.* **55**, 56–59 (2015).

60. Liu, T. et al. Promoting Proton Transfer and Stabilizing Intermediates in Catalytic Water Oxidation via Hydrophobic Outer Sphere Interactions. *Chem. Eur. J.* **28**, e202104562 (2022).

61. Carey, F. A., Sundberg, R. J. Isotope Effects, in *Advanced Organic Chemistry: Part A: Structure and Mechanisms* 222–225 (Springer US, 2007).

62. Cid, J. M. et al. Discovery of 1,4-Disubstituted 3-Cyano-2-pyridones: A New Class of Positive Allosteric Modulators of the Metabotropic Glutamate 2 Receptor. *J. Med. Chem.* **55**, 2388–2405 (2012).

63. Sheldrick, G. M. A short history of SHELX. *Acta Crystallogr. A* **64,** 112–122 (2008).

64. Spek, A. L. PLATON SQUEEZE: a tool for the calculation of the disordered solvent contribution to the calculated structure factors. *Acta Crystallogr. C* **71**, 9–18 (2015).

65. Spek, A. L. Single-crystal structure validation with the program PLATON. *J. Appl. Crystallogr.* **36**, 7–13 (2003).

66. Kunz, V. Lindner, J. O., Schulze, M., Röhr, M. I. S., Schmidt, D., Mitric, R., Würthner, F. Cooperative water oxidation catalysis in a series of trinuclear metallosupramolecular ruthenium macrocycles. *Energy Environ. Sci.* **10**, 2137–2153 (2017).

67. Meza-Chincha, A.-L. et al. Impact of substituents on molecular properties and catalytic activities of trinuclear Ru macrocycles in water oxidation. *Chem. Sci.* **11**, 7654–7664 (2020).

68. Noll, N., Würthner, F. A Calix[4]arene-Based Cyclic Dinuclear Ruthenium Complex for Light-Driven Catalytic Water Oxidation. *Chem. Eur. J.* **27**, 444–450 (2021).

Table of content figure